Mapping Hydrothermal Alteration Minerals Using Landsat 8 and ASTER Data: A Case Study from the Red Sea Hills, NE Sudan

Hydrothermal alteration minerals provide key indicators for mineral exploration, particularly in arid and inaccessible regions where field surveys are constrained. This study integrates remote sensing and GIS techniques to map alteration zones in the Red Sea Hills, NE Sudan, using Landsat 8 OLI and ASTER datasets. Preprocessing included FLAASH atmospheric correction and Minimum Noise Fraction (MNF) transformation to enhance spectral integrity. For Landsat 8 OLI, diagnostic band ratios and density slicing were applied to highlight ferric/ferrous iron oxides and hydroxyl-bearing clays, followed by supervised Parallelepiped classification of Sabins' band ratios and Crosta transformations to delineate prospective alteration zones. ASTER VNIR-SWIR data enabled higher resolution mapping through mineral indices and Spectral Angle Mapper (SAM) classification against USGS spectral library endmembers. These approaches revealed three principal hydrothermal alteration zones: phyllic (muscovite, illite), argillic (kaolinite, alunite), and propylitic (epidote, chlorite). Results demonstrate that Landsat 8 is effective for regionalscale reconnaissance, but ASTER's superior spectral resolution provides more accurate and mineralogically de-tailed alteration mapping. The study underscores the value of ASTER data for early-stage exploration in structurally complex, mineralized terranes such as the Red Sea Hills.

Keywords: Hydrothermal alteration; Remote sensing; Mineral exploration; Spectral indices; SAM classification; ASTER; Landsat 8; OLI; Arabian-Nubian Shield

Introduction

Remote sensing data from the multispectral Landsat 8 and the semi-hyperspectral ASTER sensors play an important role in locating mineral deposits and in reducing the costs associated with prospecting and exploration (Crósta and Moore, 1989; Debba et al., 2005; Carrino et al., 2015; Amer, El Mezayen and Hasanein, 2016; Alimohammadi, Alirezaei and Kontak, 2015). Although commercial mineral deposits are limited in their genetic types and modes of occurrence, a wide range of geological criteria and indicators have been established to support remote sensing techniques in identifying these deposits. These indicators, observable in spaceborne and aerial imagery, include lithological features, rock alteration patterns, structural controls, and geobotanical evidence (Hunt, 1979; Hunt and Ashley, 1979; Gupta, 2017).

Hydrothermal deposits typically form at shallow crustal depths, ranging from approximately 2 to 6 km below the surface. They are usually associated with extensive hydrothermal alteration, which is zonal in nature. This zonation progresses outward and upward from an inner potassic zone, characterized by intense alteration and dominated by biotite and K-feldspar, into phyllic, argillic, and finally propylitic zones (Mars and Rowan, 2006; Berger et al., 2014). The phyllic zone commonly consists of

sericite and pyrite-rich rocks, while the ore zone includes disseminated chalcopyrite, molybdenite, pyrite, and other sulfide minerals. Much of the ore is concentrated near the boundary between the potassic and phyllic zones, often forming a cylindrical ore shell. The argillic zone is composed of rocks enriched in alunite and kaolinite, whereas the outer propylitic zone consists of weakly altered rocks with variable mineralogy, including chlorite, epidote, and calcite (Spatz et al., 1995; Seedorff et al., 2005; Mars and Rowan, 2006). These successive alteration zones, rich in characteristic minerals, provide an essential reference for mapping hydrothermal alteration using both Landsat 8 OLI and ASTER data (Pour et al., 2018; Pour et al., 2019).

In Sudan, several studies have successfully applied multispectral data from Landsat TM, ETM+, and OLI sensors to delineate gossans, gold-bearing zones, and as-sociated sulfide mineralization. These studies have been guided by the distinct spectral signatures of gossans and alteration zones related to mineral deposits (Abdelsalam et al., 2000; El Khidir, 2006; Zeinelabdein and Albiely, 2008; El Khidir and Babikir, 2013). The Gabet Al Maadin area was selected as the study site due to the availability of previous information, particularly from remote sensing investigations using Landsat 8 and ASTER data. In addition, the region holds significant economic importance as an active and prospective mining area.

In this study, Landsat 8 OLI data, processed using various digital image processing algorithms and validated with spectral analysis of ASTER data, were used to delineate and map the alteration zones of hydrothermal minerals associated with gold-bearing sulfide deposits.

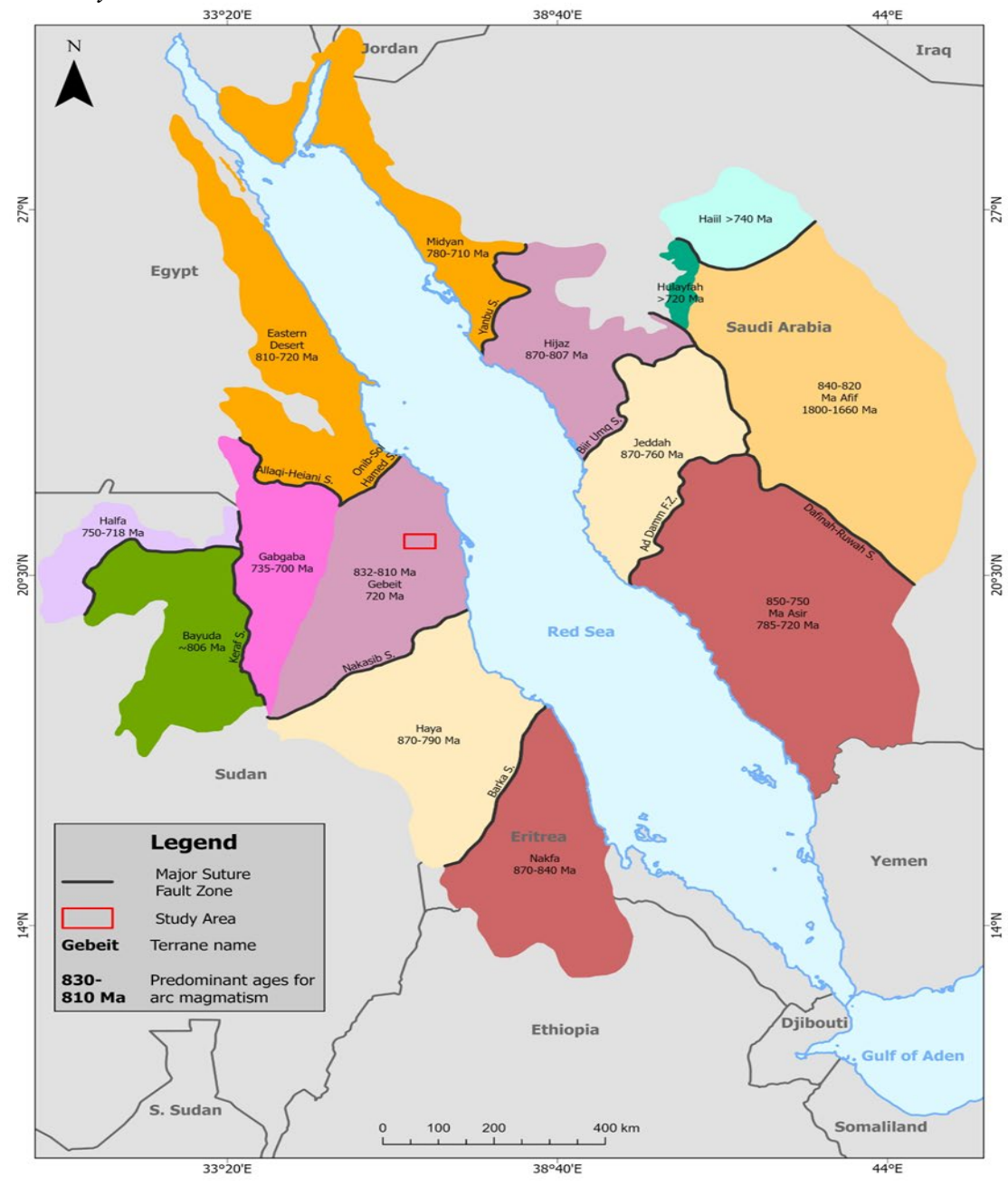
G

Geological Setting

The Red Sea Hills of Sudan form part of the Nubian Shield, which belongs to the Arabian-Nubian Shield (ANS) of northeastern Africa and the western Arabian Peninsula. The ANS extends along both sides of the Red Sea, from Egypt in the northwest, the Sinai Peninsula in the north, and Saudi Arabia in the northeast, to Ethiopia and Yemen in the southwest and southeast, respectively (Johnson, Kattan and Al-Saleh, 2004; Johnson et al., 2011). The ANS is recognized as one of the major orogenic belts formed during the Neoproterozoic assembly of Greater Gondwana. It represents an accretionary orogenic belt composed predominantly of juvenile intraoceanic island arcs, oceanic islands, and microcontinental fragments (Stern, 1994). The ANS evolved between 900 and 550 Ma as a result of the closure of the Mozambique Ocean (800-650 Ma) and the subsequent collision between East and West Gondwana (Stern, 1994; Stern, 2002).

Kröner et al. (1987) divided the Red Sea Hills into five geologically distinct terranes, separated from each other by ophiolite-decorated suture zones. The study area is located within the Gebeit Terrane (Kröner et al., 1987) (Figure 1), which comprises arc-related, low-grade volcano-sedimentary sequences and syn-tectonic igneous complexes in the area north of the Nakasib Suture (Vail, 1985; Klemenic and Poole, 1988). Whole rock Rb/Sr isochron ages of approximately 720 Ma have been reported for volcanic and plutonic rocks within the terrane (Fitches et al., 1983; Almond and Ahmed, 1987).

- 1 Figure 1. Terranes and suture zones of the Arabian–Nubian Shield, illustrating
- 2 the predominant ages of arc magmatism within each terrane and the location of
- 3 the study area



Source: Modified after (Abdelsalam, 2010)

Materials and Methods

Image Data and Data Preprocessing

Landsat 8 OLI Data

4 5

6

7 8

9

10

11

12

Landsat 8 was launched on an Atlas V rocket from Vandenberg Air Force Base, California, USA, on February 11, 2013. It is the eighth satellite in the

2025-6936-AJS - 4 NOV 2025

Landsat program, which has been continuously operated since the 1970s as a joint initiative between the U.S. Geological Survey (USGS) and NASA (Roy et al., 2014; Blondes et al., 2016). Landsat 8 carries two primary instruments: the Operational Land Imager (OLI), which acquires data in nine spectral bands spanning the visible, near-infrared (NIR), and shortwave infrared (SWIR) regions (including a panchromatic band and a cirrus band), and the Thermal Infrared Sensor (TIRS), which records two longwave thermal bands (Bands 10 and 11) (Wulder et al., 2008; Roy et al., 2014; Blondes et al., 2016).

In this study, a single optical multispectral Landsat 8 OLI scene was used, corresponding to path 172, row 45, acquired on June 5, 2025. The dataset was downloaded from the USGS Earth Resources Observation and Science (EROS) Center website.

12 13 14

15

16 17

18

19

20

21

22

23 24

25

26 27

28

29

1

2 3

4

5

6 7

8

9

10

11

ASTER Data

The Advanced Spaceborne Thermal Emission and Reflection Radiometer (ASTER) is a multispectral sensor with high spatial, spectral, and radiometric resolution (Abrams, Hook and Ramachandran, 2002). ASTER data are recorded in 14 spectral bands using three subsystems: the Visible and Near Infrared (VNIR) subsystem, consisting of three bands with wavelengths from 0.52 to 0.86 um at 15 m spatial resolution; the Shortwave Infrared (SWIR) subsystem, comprising six bands with wavelengths from 1.6 to 2.43 µm at 30 m spatial resolution; and the Thermal Infrared (TIR) subsystem, which includes five bands (Bands 10-14) spanning 8.125-11.65 µm at 90 m spatial resolution. The instrument also has along-track stereo capability, and each ASTER scene covers an area of 60×60 km², making it particularly suitable for regional mapping (Yamaguchi et al., 1999; Abrams, 2000; Yamaguchi et al., 2001; Abrams, Hook and Ramachandran, 2002).

For this research, one ASTER scene was used. The dataset (Scene ID: 00303032008081257) was acquired on August 12, 2008, and downloaded from the NASA Earthdata Search portal.

30 31 32

33

34

35

Software

36 37 38

Image processing was performed using ENVI (Environment for Visualizing Images) version 5.3 and ArcGIS version 10.8, installed on a high-performance computer. These software packages provided the necessary tools for preprocessing, spectral analysis, and spatial data integration.

Data Preprocessing

The Landsat 8 OLI data were geometrically corrected and georeferenced by the USGS prior to download. The data are provided in the Universal Transverse Mercator (UTM) coordinate system, zone 36N, based on the WGS84 datum, with all units ex-pressed in meters. Atmospheric correction was carried out using the FLAASH (Fast Line-of-sight Atmospheric Analysis of Spectral Hypercubes) model (Fraser and Green, 1987). To improve signal quality and computational efficiency, the Minimum Noise Fraction (MNF) transformation was applied, enabling dimensionality reduction, noise segregation, and optimization for subsequent image analysis (Cooley et al., 2002; Shnain et al., 2024).

Similarly, the ASTER data underwent atmospheric correction using the FLAASH technique, followed by post-processing band math to remove negative values. To enhance comparability, the six SWIR bands (30 m resolution) were resampled to match the three VNIR bands (15 m resolution), resulting in a nineband semi-hyperspectral dataset with a uniform spatial resolution of 15 m (Shnain et al., 2024).

Landsat 8 OLI data for mineral prospecting

Landsat 8 data are considered fundamental for mineral prospecting, especially in remote or inaccessible regions. They are extremely useful during the systematic exploration phase of mining and are widely applied to geological mapping and mineral exploration worldwide (Safari, Maghsoudi and Pour, 2018; Mwaniki, Möller and Schellmann, 2015). The OLI spectral range (0.325–2.5 µm) records solar-reflected light and includes several diagnostic absorption features of alteration minerals. These features are related to vibrational overtones, electronic transitions, charge transfer, and conduction processes (Sabins and Lulla, 1987).

In this study, Landsat 8 OLI data were processed using two complementary approaches: (i) the band ratio technique, and (ii) supervised classification applied to Sabins' band ratios and to the Feature Oriented Principal Component Selection (FOPCS) method. Both approaches were used to delineate hydrothermal alteration zones (Sabins and Lulla, 1987).

The band ratio process for mineral prospecting

Band ratioing is one of the most effective techniques for detecting alteration minerals such as ferrous and ferric iron oxides, as well as hydroxyl-bearing minerals (Sabins and Lulla, 1987; Zhang, Pazner and Duke, 2007). Band ratio images are generated by dividing the digital number (DN) values of one spectral band by those of another (Sabins, 1999; Lillesand, Kiefer and Chipman, 2015). These images enhance spectral differences between minerals, minimize the influence of topography and solar illumination, and highlight absorption features associated with alteration. Gray-scale ratio images display pixels with the largest differences in reflectance between two bands. Band ratios are therefore widely used to emphasize iron oxide and clay or hydroxyl-bearing minerals, which are critical indicators of hydrothermal alteration (Gupta, 2017) [6]. To further enhance interpretation, density slicing was applied, converting the continuous

tonal variations of the ratio images into discrete intervals corresponding to specified DN ranges (Sabins and Lulla, 1987; Zhang, Pazner and Duke, 2007).

Supervised classification

Supervised classification is another powerful remote sensing technique for mapping mineral alteration zones. It involves the selection of sample Regions of Interest (ROIs) and the extraction of their spectral signatures across all bands. These signatures are used to compute statistical parameters that guide classification algorithms. In this study, the Parallelepiped classifier was used to assign each pixel to the most probable class, enabling accurate and detailed thematic mapping (Richards, 2022; Lillesand, Kiefer and Chipman, 2015). Supervised classification was applied to false-color composite (FCC) images generated from Sabins' band ratios and from the FOPCS method to identify hydrothermal alteration zones.

Sabins' band ratio FCC image

The Sabins' FCC image was produced by assigning the band ratios 6/7, 4/6, and 4/2 to the red, green, and blue channels, respectively (Sabins, 1999). This combination enhances the spectral expression of alteration minerals. The 6/7 ratio highlights clay-rich zones, since clay minerals show strong reflectance in Band 6 (SWIR1) and low reflectance in Band 7 (SWIR2), which appear reddish in the composite. The 4/2 ratio enhances iron oxide-bearing areas, reflecting the absorption features in the blue region (Band 2) and the high reflectance in the red region (Band 4). These spectral properties allow iron-bearing minerals to be clearly distinguished (Pour and Hashim, 2012a; 2012b).

The Feature Oriented Principal Component Selection (FOPCS) process

The FOPCS method, also referred to as the Crosta technique, is a targeted principal component analysis (PCA) approach that uses only a subset of bands selected to emphasize spectral features of interest (Crósta, 1989; Loughlin, 1991; Crósta et al., 2003). In this study, two band combinations were analyzed: the Himage, designed to enhance hydroxyl-bearing and clay minerals, and the Fimage, intended to highlight iron oxide signatures. The eigenvector loadings of the resulting principal components were carefully examined to determine which components best represent the spectral properties of alteration minerals (Zhang, Pazner and Duke, 2007).

ASTER data for mineral prospecting

ASTER data, with their high spatial and spectral resolution, provide valuable coverage for identifying hydrothermal alteration minerals and lithological units (Cooley et al., 2002). Hydrothermal alteration zones such as phyllic, argillic, and propylitic can be distinguished by their characteristic absorption features within ASTER's spectral range. Specifically, the phyllic alteration zone, dominated by illite and muscovite (sericite), is characterized by a strong Al-OH absorption feature centered at 2.20 µm, which coincides with ASTER Band 6. The argillic zone, comprising kaolinite and alunite, shows a

2025-6936-AJS - 4 NOV 2025

secondary Al-OH absorption feature at 2.17 μ m, corresponding to ASTER Band 5. The propylitic zone, characterized by chlorite and epidote, exhibits absorption features near 2.35 μ m, coinciding with ASTER Band 8 (Mars and Rowan, 2006; Pour et al., 2018; Testa et al., 2018).

In the present study, ASTER VNIR and SWIR data were analyzed using two methods: mineral indices derived from band ratios and the Spectral Angle Mapper (SAM) classifier. Both approaches were applied to detect illite, muscovite, kaolinite, alunite, epidote, and chlorite, which are diagnostic minerals of phyllic, argillic, and propylitic alteration zones.

Mineral indices

Mineral indices were calculated by applying specific band ratios that target diagnostic absorption features of selected minerals Rowan and Mars, 2003; Rowan et al., 2003). Preprocessing of the ASTER dataset included radiometric calibration and atmospheric correction of VNIR and SWIR bands. Lithological indices were also derived for the TIR bands, based on the distinct spectral properties of various minerals and rock types (Ninomiya, 2003; Van der Meer et al., 2012).

Three indices were particularly applied in this study:

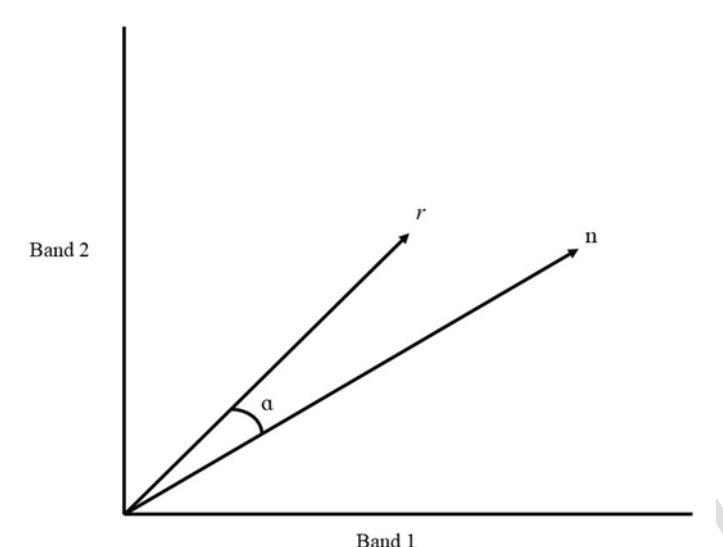
21 Muscovite Index =
$$\frac{Band 7}{Band 6}$$

22 Alunite Index = $\frac{Band 7}{Band 5} \times \frac{Band 7}{Band 8}$
23 Kaolinite Index = $\frac{Band 4}{Band 5} \times \frac{Band 8}{Band 6}$

Spectral Angle Mapper (SAM) Classifier

The SAM technique classifies pixels based on their spectral similarity to known reference spectra (Rajendran et al., 2013). Each pixel's spectral vector is compared to library spectra of known minerals, and the similarity is quantified by measuring the angle between the vectors. Smaller angles indicate greater similarity. This procedure produces a spectral similarity map, in which each pixel is classified according to its closest match from the spectral library. The SAM output includes a classified image displaying the distribution of alteration minerals and rule images showing the angular distance (in radians) between pixel spectra and reference spectra (Kruse et al., 1993; Rowan and Mars, 2003; Van der Meer et al., 2012).

Figure 2. Two-dimensional illustration of spectral vectors r (reference spectrum) and n (pixel spectrum), showing the spectral angle (a) between them



Source: Modified after (Kruse et al., 1993).

Results

Landsat 8 OLI data processing for mineral prospecting

Multispectral Landsat 8 OLI data were processed to delineate and map alteration zones associated with mineralization. These zones are defined by the presence of key alteration minerals, including ferric and ferrous iron oxides such as hematite, goethite, and limonite, as well as clay and hydroxyl-bearing minerals such as kaolinite, montmorillonite, illite, and alunite. The diagnostic spectral features of these minerals serve as important indicators for identifying potential mineral deposits within a multispectral remote sensing framework. To avoid misinterpretation, alluvial wadi deposits were masked during the analysis, since they often contain weathered, altered, and fragmented rock material whose spectral signatures can obscure or distort the signals of the targeted alteration minerals.

Band ratio images

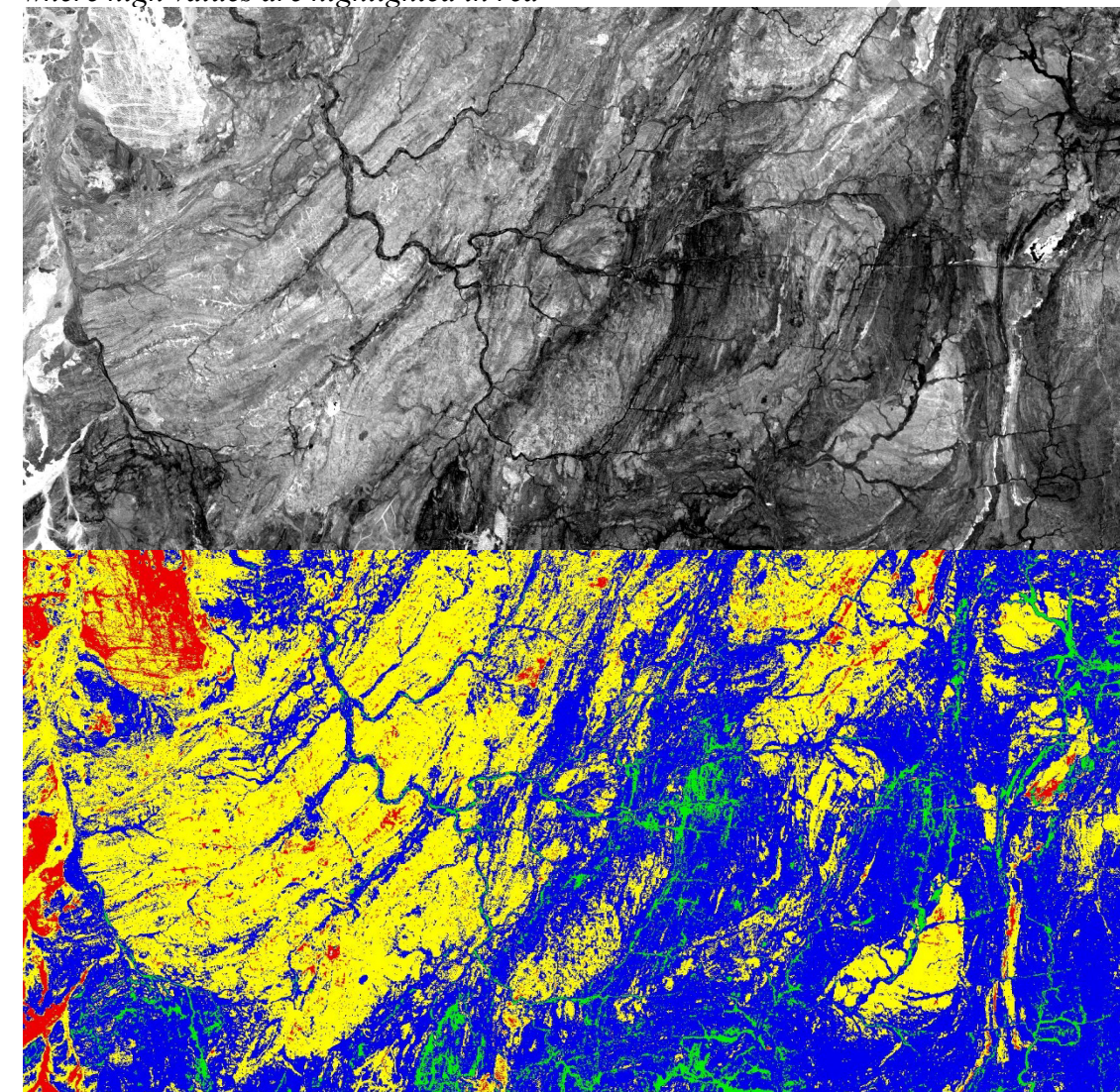
Selective band ratios were applied to highlight hydrothermal alteration zones. Ratios 4/2, 6/5, and 6/7 were specifically used to identify ferrous iron oxides, ferric iron oxides, and hydroxyl-bearing minerals, respectively. A low-pass filter was first applied to the ratio images to reduce noise. The resulting grayscale images were further enhanced through density slicing, which emphasized the spectral responses associated with the target minerals. Finally, the density-sliced results were converted into vector classes, allowing the delineation and mapping of distinct alteration zones.

Ferrous iron oxides and ratio

Ferrous iron oxides are characterized by high reflectance in the red portion of the spectrum (Band 4) and low reflectance in the blue region (Band 2) of Landsat 8 OLI data. For this reason, the band ratio 4/2 was used to delineate areas enriched in ferrous iron oxides. In the grayscale display, ferrous-rich areas appear in light tones, while in the density-sliced output they are highlighted in red (Figure 3a, b).

Figure 3. Band ratio 4/2 image used for mapping ferrous oxides: (a) grayscale display, where high values appear as bright tones; (b) density-sliced display,

where high values are highlighted in red



Source: Authors own elaboration

Ferric iron oxides band ratio

Ferric iron oxides show diagnostic absorption in the near-infrared region (Band 5) and high reflectance in the shortwave infrared region (Band 6). Consequently, the band ratio 6/5 effectively delineates ferric oxide-rich areas. These appear in light tones in the grayscale image and are displayed in red hues in the density-sliced image (Figure 4a, b).

6 7 8

9

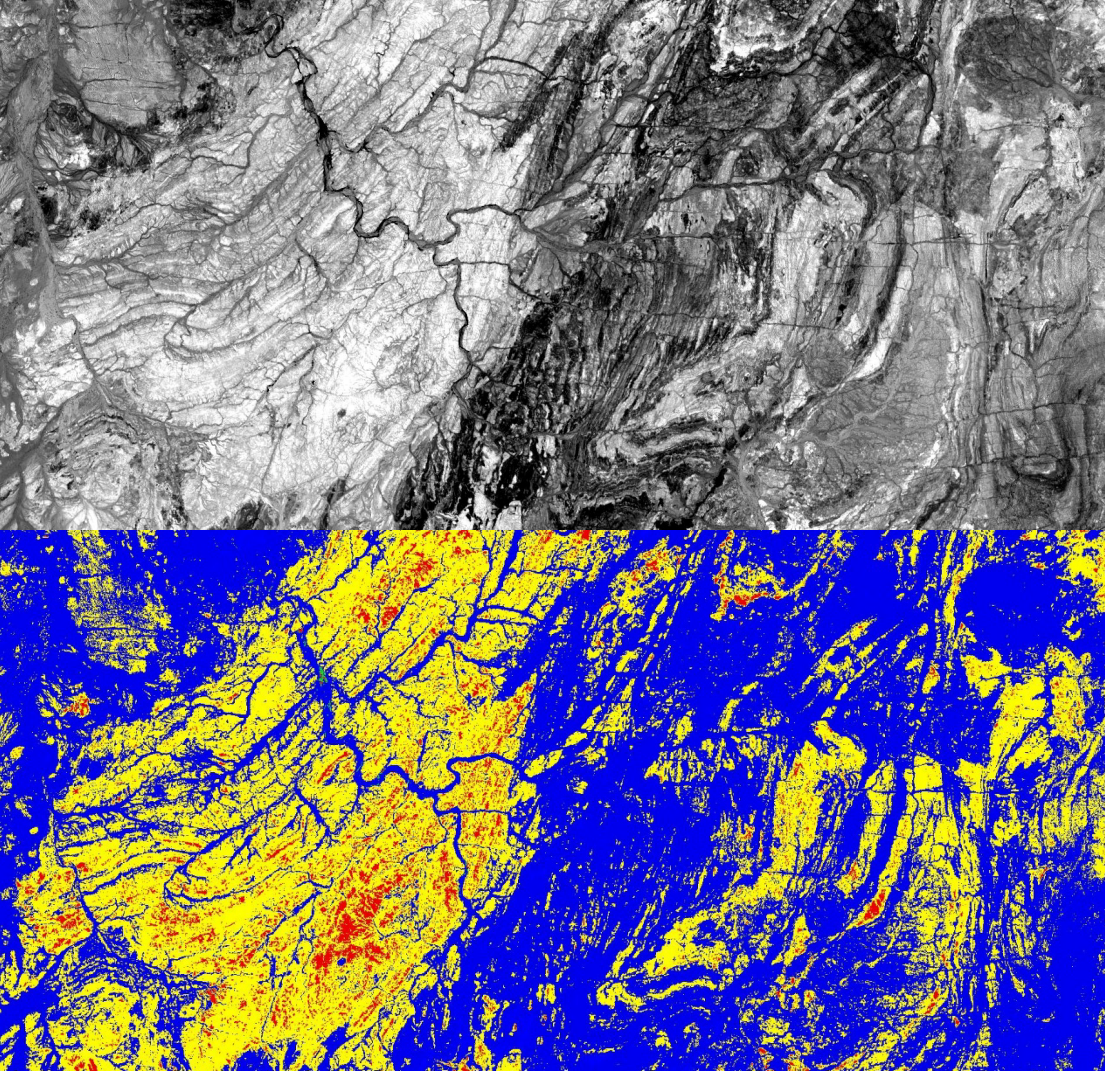
2 3

4

5

Figure 4. Band ratio 6/5 image used for mapping ferric oxides: (a) grayscale display, where high values ap-pear as bright tones; (b) density-sliced display,

where high values are highlighted in red 10



12 13

11

Source: Authors own elaboration

14 15

Hydroxyl bearing band ratio

Hydroxyl-bearing alteration minerals, including clays, micas, and 16 amphiboles, exhibit distinct absorption features in the SWIR-2 region (Band 7) 17 18 due to the strong Al - OH and Mg-OH vibrational absorptions. At the same time, they show high reflectance in the SWIR-1 region (Band 6). Accordingly, the 19

band ratio 6/7 was used to identify hydroxyl-bearing mineral assemblages. In the outputs, these zones appear in bright tones in the grayscale image and in red hues in the density-sliced version (Figure 5a, b).

Figure 5. Band ratio 6/7 image used for mapping clay minerals: (a) grayscale display, where high values appear as bright tones; (b) density-sliced display, where high values are highlighted in red

Source: Authors own elaboration

GIS spatial analysis

The band ratio images derived from ratios 4/2, 6/5, and 6/7 revealed three distinct types of potential alteration zones. Each was extracted as a separate class through density slicing and subsequently converted into vector format within a GIS environment. As shown in Figure 6a, ferrous oxide zones are represented in blue, ferric oxide zones in green, and clay-rich (hydroxyl-bearing) zones in red. To identify the most prospective zones of hydrothermal alteration, a spatial intersection analysis was carried out. This procedure highlighted the areas of

1

overlap among the three classes, rep-resenting the zones with the highest probability of being associated with hydrothermal mineralization. These priority targets are displayed in yellow in Figure 6b.

Figure 6. (a) Alteration zones overlaid on the satellite image, showing high values of the band ratio images: 6/7 for clay minerals (red), 4/2 for ferrous oxides (blue), and 6/5 for ferric oxides (green). (b) Spatial intersection analysis of the vectorized anomalous values from the band ratios, highlighting the overlapping alteration zones in yellow

10 36°27'0"E

11 12 13

Source: Authors own elaboration

Supervised classification

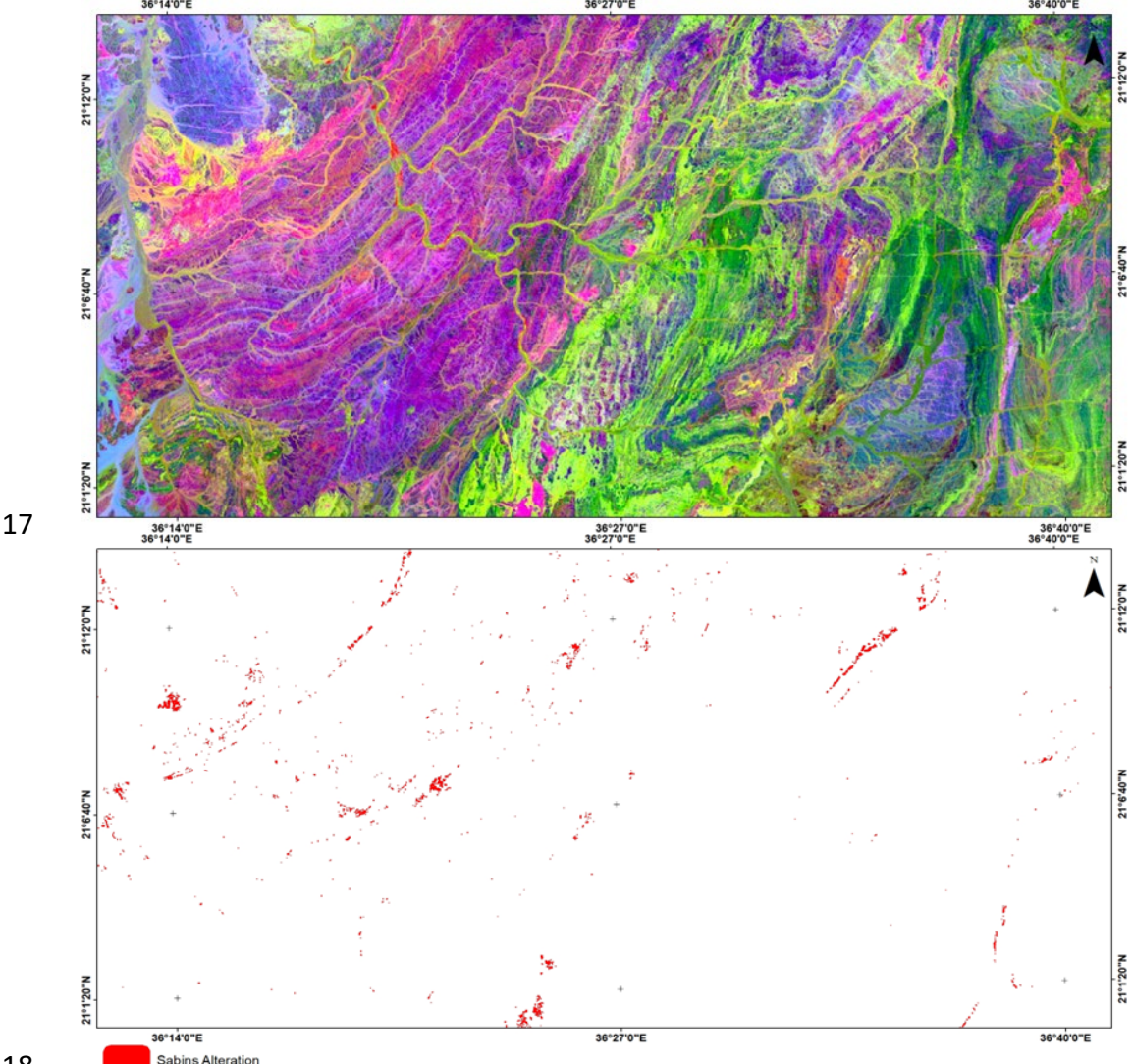
14 15 16

In Supervised classification using the Parallelepiped method was applied to identify hydrothermal alteration zones in both Sabins' and Crosta FCC images.

Sabins' band ratio FCC image

The Sabins' FCC image was generated by assigning the band ratios 6/7, 4/6, and 4/2 to the red, green, and blue channels, respectively (Sabins and Lulla, 1987). The 6/7 ratio highlights clay-rich minerals, which show high reflectance in Band 6 (SWIR1) and low reflectance in Band 7 (SWIR2), resulting in reddish hues in the composite. Areas enriched in iron oxides are emphasized by the 4/2 ratio, which exploits strong absorption in Band 2 (blue) and high reflectance in Band 4 (red), producing blue hues. The 4/6 ratio is particularly effective for mapping ferrous iron oxides and appears in green hues. Collectively, the Sabins' FCC image provides a clear delineation of hydrothermal alteration zones associated with mineralization, which are represented by crimson -orange hues (Figure 7).

Figure 7. Sabins' FCC image showing alteration zones associated with mineralization, displayed in crimson-orange hues; (b) classified alteration zones derived from the Sabins' band ratio image, displayed in red



Source: Authors own elaboration

Feature Oriented Principal Component Selection (FOPCS)

The Feature Oriented Principal Component Selection (FOPCS), also known as the Crosta FCC method, is designed to emphasize only those spectral bands that contain diagnostic absorption features of iron oxides and clay-bearing minerals. For Landsat 8 OLI data, the bands selected for mapping clay-bearing minerals were Bands 2, 5, 6, and 7, whereas Bands 2, 4, 5, and 7 were chosen for detecting iron oxides.

H image (The Hydroxyl bearing and clay minerals)

The H-image is produced from principal component analysis (PCA). In general, PC1 accounts for overall albedo of the selected bands and thus contains minimal spectral variability, while PC2 reflects the contrast between the NIR and SWIR regions. In this study, eigenvector analysis (Table 1) indicated that PC3 and PC4 were the most effective components for delineating zones enriched in clay and hydroxyl-bearing minerals.

Table 1. Eigenvector statistics of principal components used for hydroxylbearing mineral mapping (H-image, FOPCS method)

Eigenvector	Band 2	Band 5	Band 6	Band 7
PC 1	0.168356	0.432960	0.667114	0.582374
PC 2	0.463554	0.725617	-0.169314	-0.479510
PC 3	0.613774	-0.151658	-0.540803	0.554810
PC 4	0.616486	-0.512859	0.483553	-0.350851

Source: Authors own elaboration

In this case, PC4 exhibited the strongest contrast between Bands 6 and 7, with Band 6 showing a strong positive loading and Band 7 a strong negative loading. This contrast makes PC4 particularly sensitive to hydroxyl-bearing minerals. To enhance the mapping of these minerals, which appear as dark pixels in the PC4 image, the image was negated (255 - DN), followed by the application of a low-pass filter to reduce noise. The resulting processed image is referred to as the H-image.

F image (The iron oxides rich areas)

The FOPCS transformation applied to Bands 2, 4, 5, and 7 produced the F-image. Eigenvector analysis (Table 2) indicated that either PC2 or PC4 effectively isolates iron oxide-rich zones due to the strong contrast observed among the visible bands, which is diagnostic of ferric iron minerals.

Table 2. Eigenvector statistics of principal components used for iron oxide mapping (F-image, FOPCS method)

Eigenvector	Band 2	Band 4	Band 5	Band 7
PC 1	0.224696	0.476917	0.536085	0.659298
PC 2	0.312708	0.443982	0.389090	-0.744112
PC 3	0.736766	0.214905	-0.632033	0.107361
PC 4	-0.555789	0.727493	-0.402189	-0.009802

Source: Authors own elaboration

3

4

5 6

7

8

9

10

PC4 exhibited the greatest contrast in eigenvector loadings between Bands 4 and 2, making it particularly effective for mapping ferric iron oxide minerals. PC4 was therefore selected as the F-image, and a low-pass filter was applied to reduce noise, resulting in the final F-image.

The Crosta composite image (FCC) was then generated by assigning the hydroxyl-sensitive image (H-image) to the red channel, the iron oxide-sensitive image (F-image) to the blue channel, and a mathematically combined image (Himage + F-image) to the green channel. This composite effectively highlights alteration zones enriched in both iron oxides and clay minerals, which appear in whitish-yellow hues (Figure 8).

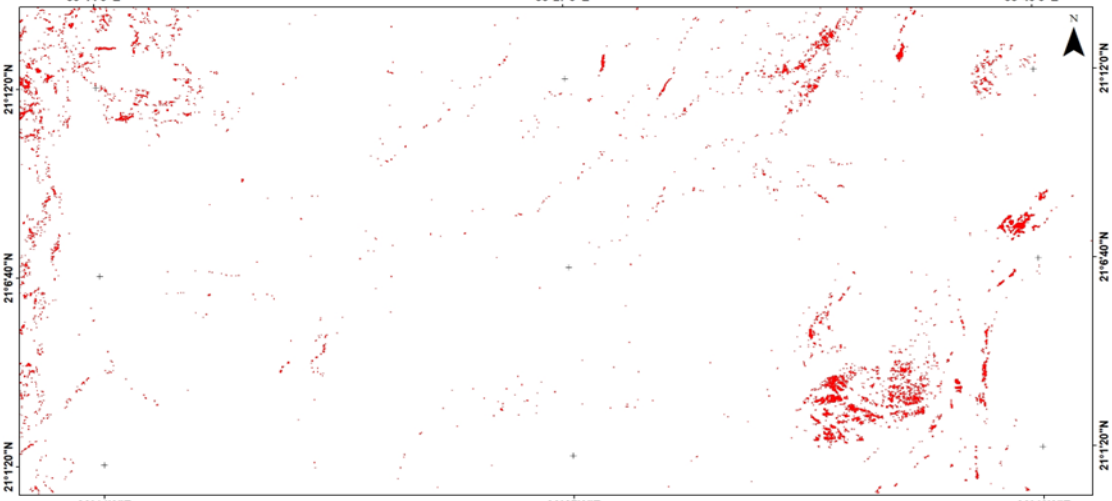
11 12 13

14

Figure 8. (a) Crosta FCC image showing alteration zones associated with mineralization, displayed in whitish - yellow hues; (b) classified alteration zones derived from the Crosta FCC image, displayed in red

15

16



17 18

Source: Authors own elaboration

Crosta Alteration

GIS spatial analysis

The alteration classes obtained from the supervised classification of both Sabins' and Crosta composites were converted into vector format for integration within a GIS environment. A spatial intersection analysis was then performed on the vectorized alteration zones, enabling the delineation of highly probable alteration zones. These priority zones are highlighted in red in (Figure 9).

Figure 9. (a) Classified alteration zones derived from the Sabins' and Crosta methods overlaid on the FCC image; (b) alteration map generated through spatial intersection of the Sabins' and Crosta composites, with the most probable alteration zones displayed in red

Alteration 21°1'20"N 36°27'0"E

Source: Authors own elaboration

ASTER data processing for mineral prospecting

This section presents the application of two methods to ASTER VNIR-SWIR data for mapping hydrothermally altered minerals: (i) spectral band ratio indices and (ii) spectral analysis using the SAM classifier. These methods target minerals such as illite, muscovite, kaolinite, alunite, epidote, and chlorite, which display distinctive absorption and reflectance features, allowing the identification and delineation of hydro-thermal alteration zones, including phyllic, argillic, and propylitic zones.

Figure 10. False color composite (FCC) of ASTER bands 4, 6, and 8 displayed in red, green, and blue channels, respectively, for the study area



Source: Authors own elaboration

Mineral indices

Mineral indices were derived by applying spectral band ratios targeting the diagnostic absorption features of selected minerals. The indices used in this study include the Muscovite Index, the Alunite Index and the Kaolinite Index.

Muscovite Mapping

The Muscovite Index highlights the absorption feature at 2.20 µm (ASTER Band 6), corresponding to Al-OH bearing minerals that define phyllic alteration zones. In the grayscale index image, muscovite-rich areas appear as bright tones, concentrated mainly in the upper left part of the study area and extending along a NNE structural trend. Additional occurrences are observed in the central lower region and near the upper right corner, also aligned with the main NNE trend. The thresholded, color-coded image and its vectorized results highlight these muscovite-rich zones in red, delineating phyllic alteration zones (Figure 11a, b).

Alunite Mapping

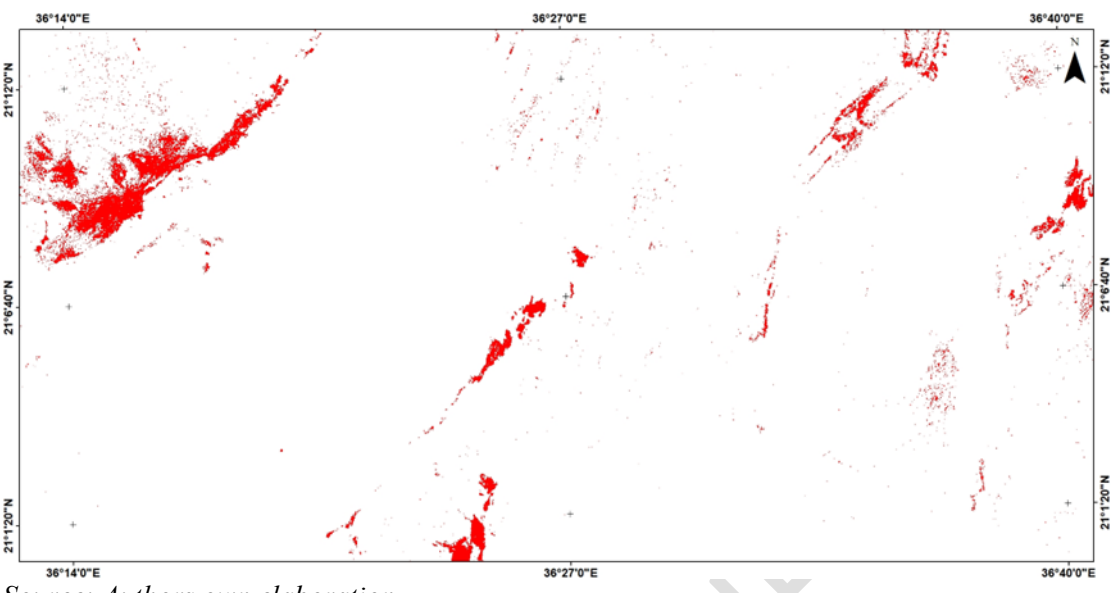
The Alunite Index delineates the argillic alteration zones containing alunite and kaolinite minerals, which exhibit AL-O-H absorption features at 2.20 and $2.17 \,\mu m$ (ASTER band 5), respectively. The Alunite Index image shows brighter tone in the greyscale image distributed in the upper left corner of the image, extending along with a NNE trend, the rest values are observed in the central lower part with the main NNE trend of the study area see Figure 12 a. The thresholding high value color coded image and vectorized results appear in blue color mapping the phyllic alteration zones Figure 12 b.

Kaolinite Mapping

The Kaolinite Index delineates zones enriched in kaolinite, which define argillic alteration. In the grayscale display, kaolinite-rich zones appear as bright tones, concentrated in the upper left part of the study area and extending along the NNE structural trend. Additional occurrences are observed in the central upper and lower regions and near the upper right corner, all aligned with the same structural trend. In the color-coded and vectorized image, kaolinite-rich zones are mapped in green (Figure 13a, b).

Figure 11. 11 Muscovite Index derived from ASTER data: (a) band ratio image (Band 7 / Band 6), highlighting muscovite-rich zones; (b) vectorized output of mapped muscovite, displayed in red

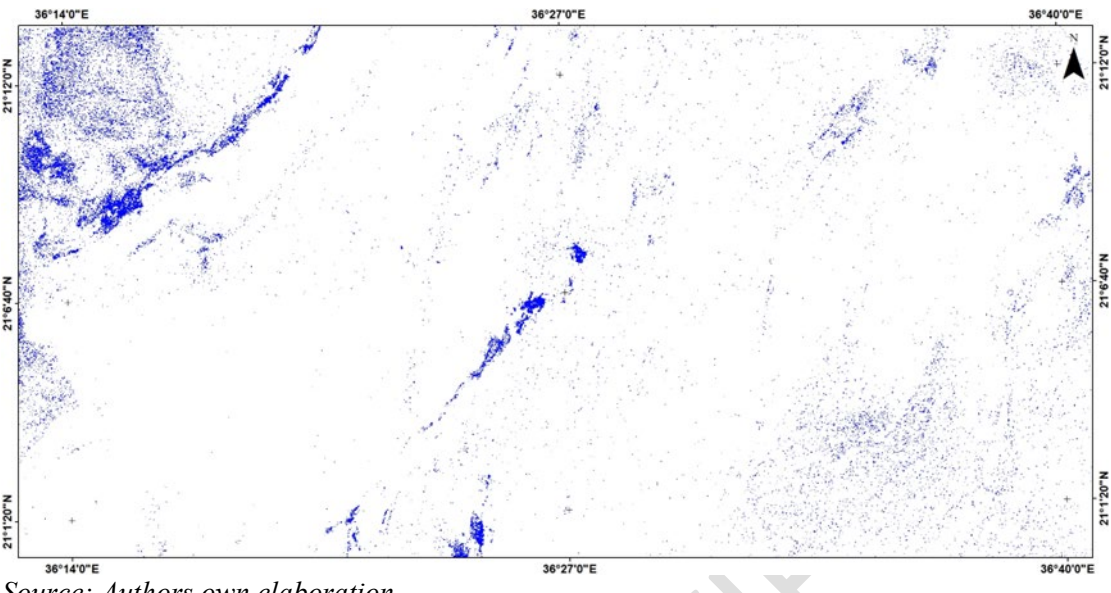




Source: Authors own elaboration

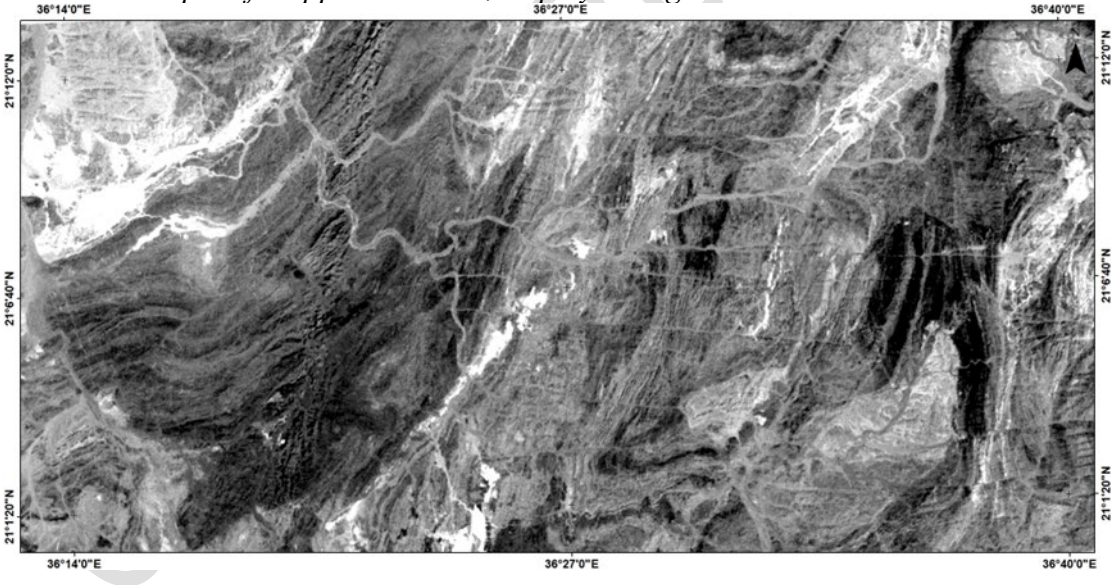
Figure 12. Alunite Index derived from ASTER data: (a) band ratio image ((Band 7 / Band 5) × (Band 7 / Band 8)), highlighting alunite-rich zones; (b) vectorized output of mapped alunite, displayed in blue



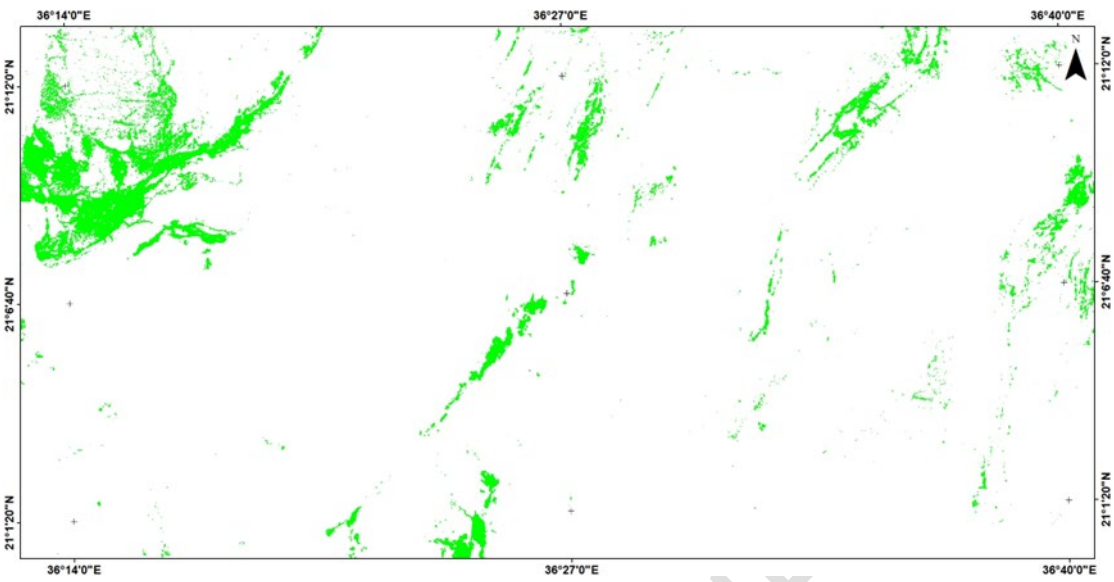


Source: Authors own elaboration

Figure 13. Kaolinite Index derived from ASTER data: (a) band ratio image $((Band\ 4\ /\ Band\ 5)\ \times\ (Band\ 8\ /\ Band\ 6))$, highlighting kaolinite-rich zones; (b) vectorized output of mapped kaolinite, displayed in green



2

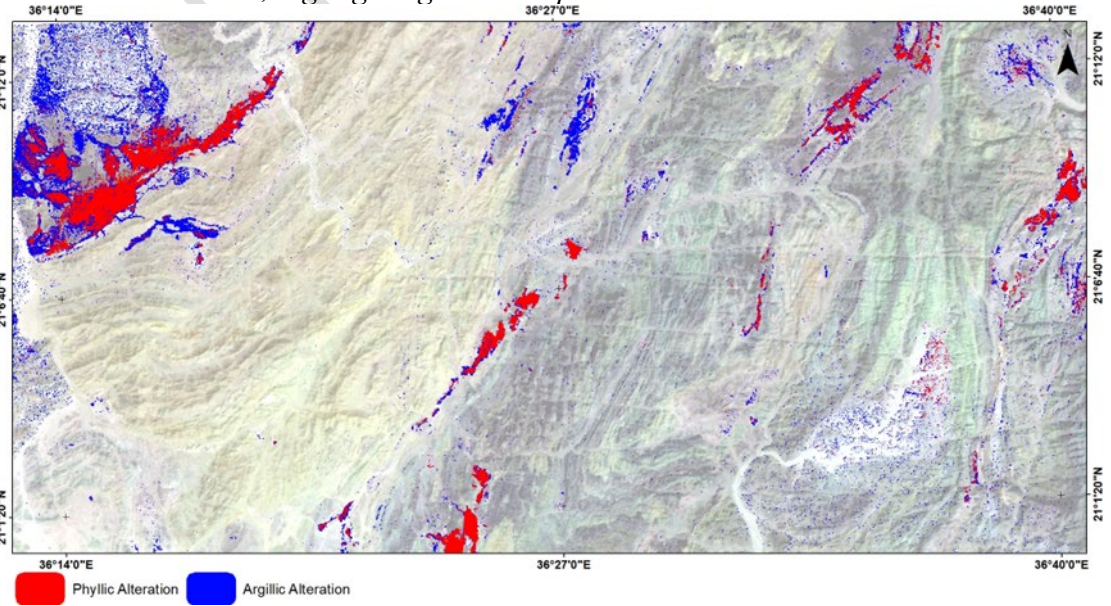


Source: Authors own elaboration

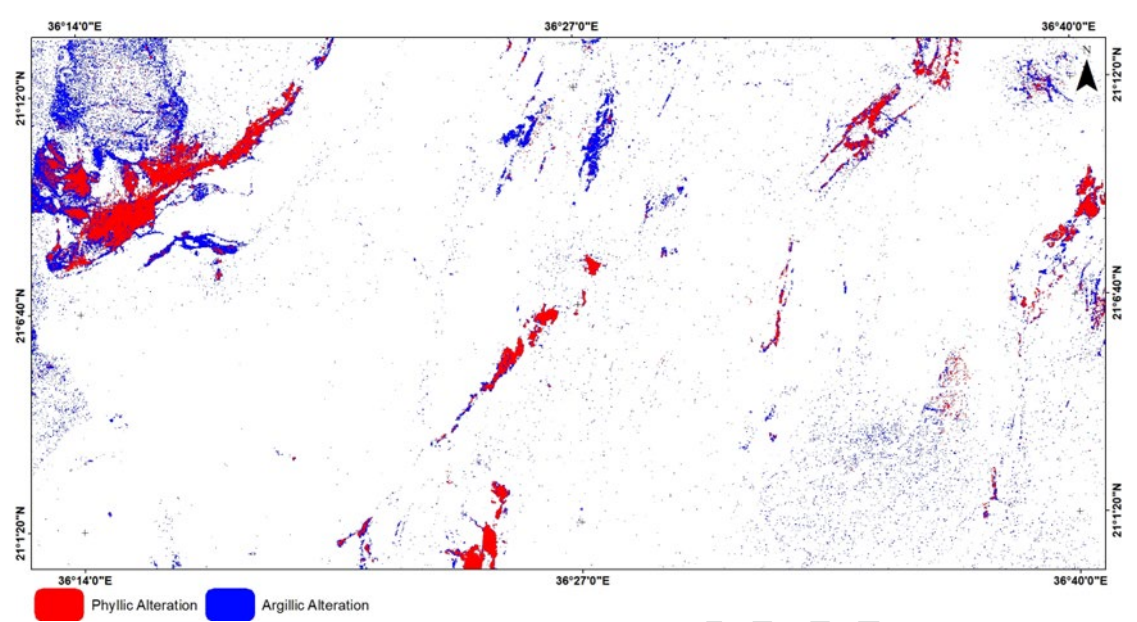
GIS spatial analysis

The vectorized results of the mineral indices were integrated within a GIS environment to highlight areas with overlapping phyllic and argillic alteration zones, which serve as indicators of potential mineralization. The analysis revealed that the upper left corner of the study area represents the most probable zone for mineralization, owing to the strong concentration of alteration signatures. Additional zones of high index values were also identified in the central lower region and near the upper right corner of the study area, all aligned with the dominant NNE structural trend (Figure 14).

Figure 14. (a) Overlay of combined phyllic and argillic alteration zones on the FCC image; (b) integrated results of phyllic and argillic alteration zones derived from mineral indices, highlighting the most probable mineralized zones



2025-6936-AJS - 4 NOV 2025

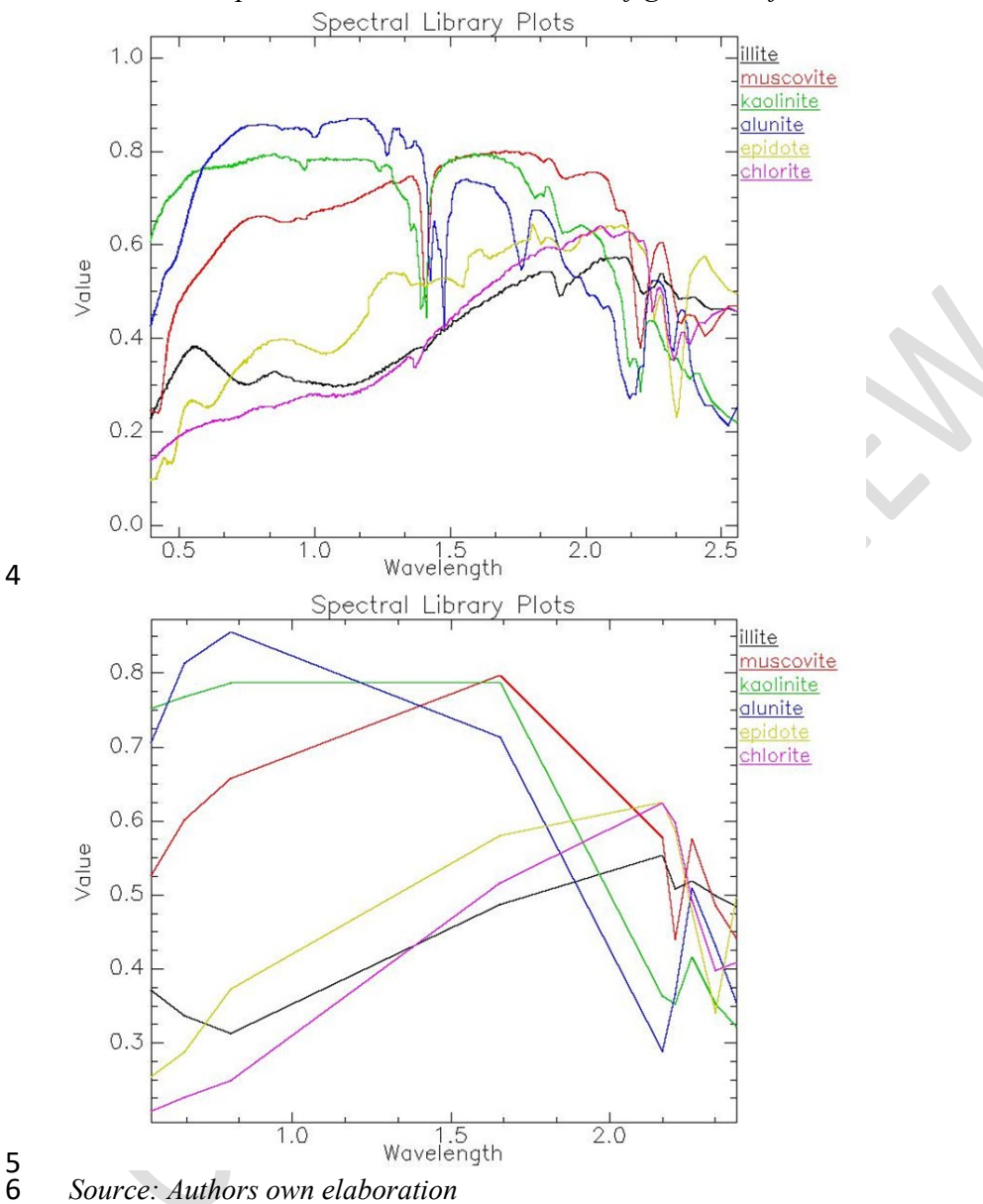


Source: Authors own elaboration

Spectral Angle Mapper (SAM) Classifier

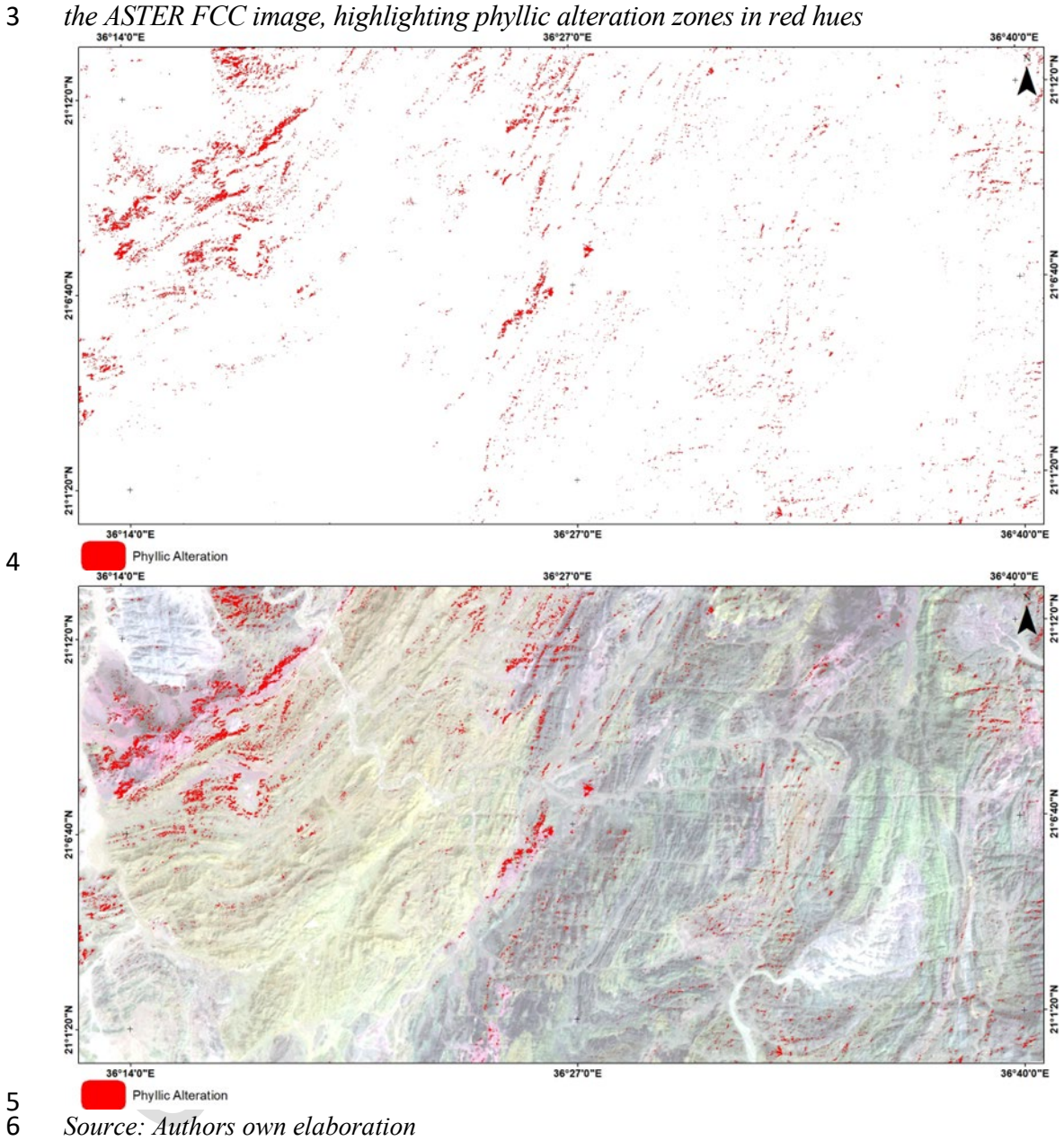
The Spectral Angle Mapper (SAM) algorithm compares the spectral signature of a target object with reference spectra obtained from standardized laboratory spectral libraries, such as those provided by the USGS. In this study, spectra of common hydrothermal alteration minerals associated with mineralization, specifically illite, muscovite, kaolinite, alunite, epidote, and chlorite, were selected from the USGS spectral library (Figure 15a). These reference spectra were subsequently resampled to match the spectral resolution and band configuration of the ASTER sensor (Figure 15b).

Figure 15. (a) Laboratory spectra of hydrothermal alteration minerals from the USGS spectral library used in this study; (b) the same reference spectra resampled to match the spectral resolution and band configuration of ASTER bands



Rule images were generated to highlight the surface distribution of the selected spectra. The SAM algorithm applies a default threshold value, but in this case thresh-olds behave differently because lower values indicate a higher probability of a pixel belonging to the target class in the SAM rule image. Therefore, manual adjustment of the threshold was performed based on visual interpretation. The SAM-derived illite and muscovite images delineate phyllic alteration zones, which are represented in red. These zones are concentrated in the upper left corner of the study area and extend into the upper and central parts of the region (Figure 16).

Figure 16. SAM classifier results from ASTER data: (a) combined distribution of illite and muscovite, displayed in red; (b) combined illite and muscovite overlaid on the ASTER FCC image, highlighting phyllic alteration zones in red hues



Source: Authors own elaboration

For kaolinite and alunite, the classified image highlights areas of high values corresponding to argillic alteration zones. These zones are represented in green and are mainly concentrated in the upper left corner of the study area, with more limited occurrences observed in the central region (Figure 17).

11 12 13

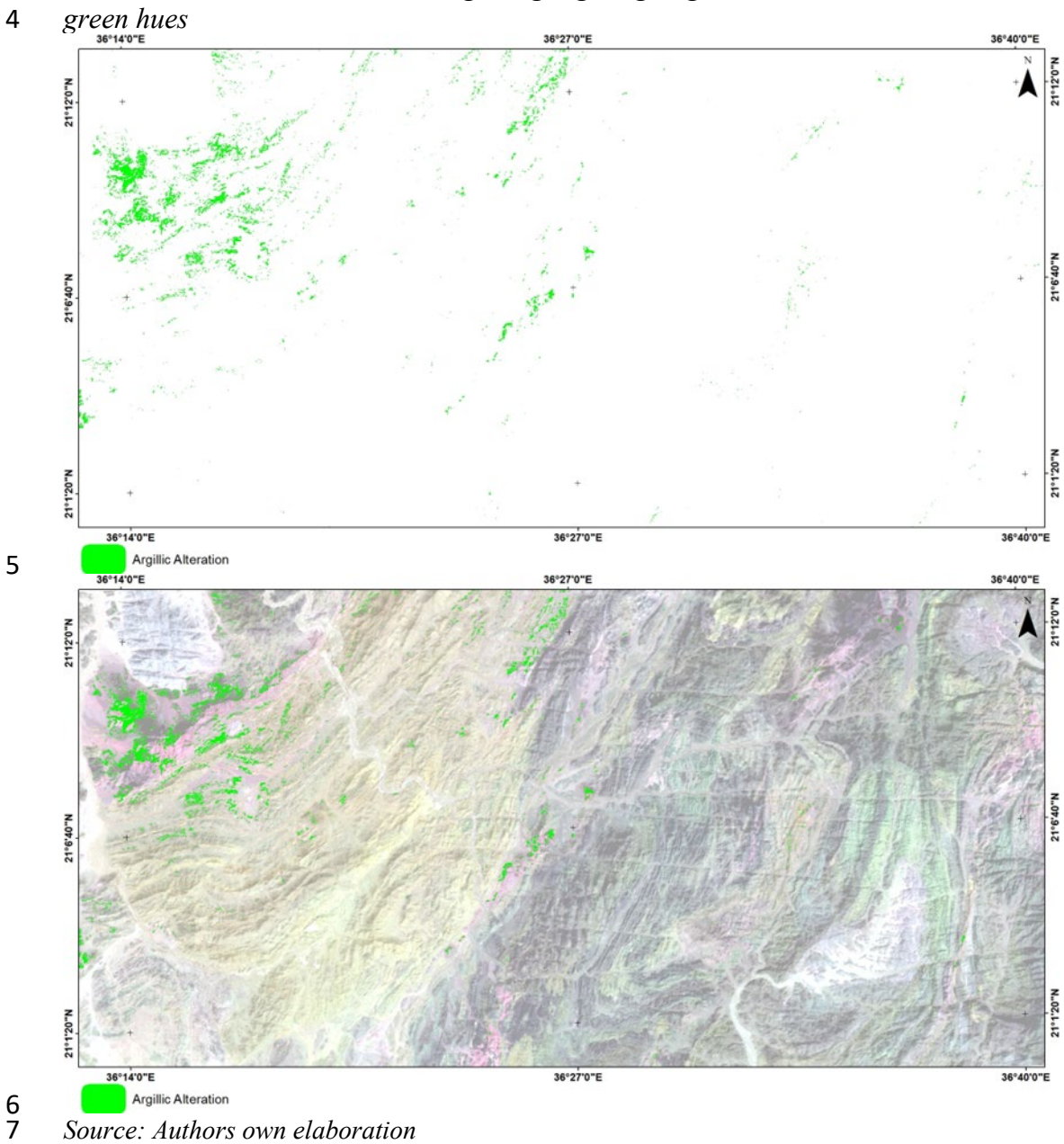
7 8

9

10

1

Figure 17. SAM classifier results from ASTER data: (a) combined distribution of kaolinite and alunite, dis-played in green; (b) combined kaolinite and alunite overlaid on the ASTER FCC image, highlighting argillic alteration zones in



Source: Authors own elaboration

The SAM classification of epidote and chlorite was used to map propylitic alteration zones. These zones are represented in blue and are primarily concentrated in the left-central part of the study area (Figure 18).

12 13

8

9

10

11

1

2

Figure 18. Figure 18. SAM classifier results from ASTER data: (a) combined distribution of epidote and chlorite, displayed in blue; (b) combined epidote and chlorite overlaid on the ASTER FCC image, high lighting propylitic alteration

zones in blue hues

Propylitic Alteration Source: Authors own elaboration

GIS Spatial Analysis

5

6 7

8 9

10

11

12

13

14

15

The SAM classification successfully mapped hydrothermal alteration minerals, delineating phyllic, argillic, and propylitic zones. The resulting images illustrate the spatial distribution of these zones based on the diagnostic absorption features of their respective endmember minerals. The classified pixels were exported as shapefiles representing the extent of each alteration type. Spatial analysis was then conducted on these shapefiles to extract and delineate

the most probable hydrothermal alteration zones associated with mineralization (Figure 19a).

The results of the ASTER SAM spectral analysis revealed several probable alteration zones within the study area. These zones are primarily concentrated in the upper left corner, aligned with a NNE structural trend, with additional occurrences in the central region and smaller, scattered zones in the upper middle part of the area (Figure 19b).

Figure 19. Results of SAM classification applied to ASTER VNIR-SWIR data: (a) alteration map showing phyllic (red), argillic (green), and propylitic (blue) zones; (b) ASTER FCC image (bands 4, 6, and 8 in RGB) overlaid with SAM-derived alteration zones

12 derived alteration zones

MANTE M

Source: Authors own elaboration

Discussion

 The spectral characteristics of hydrothermal alteration zones were investigated using both Landsat 8 OLI and ASTER data. For Landsat 8 OLI, band ratio techniques were applied, specifically ratios 4/2, 6/5, and 6/7, to identify ferrous iron oxides, ferric iron oxides, and clay (hydroxyl-bearing) minerals, respectively. The resulting grayscale and density-sliced images delineated distinct alteration zones, which were further analyzed in a GIS framework to highlight the most probable mineralized areas. Supervised classification was also performed using the Parallelepiped classifier, with training samples derived from alteration zones identified in the Sabins' FCC band ratio composite and the Crosta (FOPCS) method. The classified outputs from both approaches were integrated in a GIS environment to extract the most reliable alteration zones within the study area.

For ASTER data, VNIR and SWIR mineral indices were used to detect phyllic alteration through the mapping of muscovite, and to identify argillic alteration zones by detecting kaolinite and alunite. In addition, the SAM classifier was applied to match the spectral signatures of indicator minerals with reference spectra from the USGS spectral library. This process successfully distinguished three main hydrothermal alteration zones: phyllic (illite and muscovite), argillic (kaolinite and alunite), and propylitic (epidote and chlorite).

Overall, the results demonstrate that ASTER data provide superior capabilities for hydrothermal mineral prospecting compared to Landsat 8 OLI data. The higher spectral resolution of ASTER allows more effective identification of diagnostic minerals and their spatial distribution. These findings confirm that ASTER is a valuable tool in the early stages of mineral exploration, offering a rapid, cost-effective, and reliable approach for identifying prospective zones associated with hydrothermal alteration minerals.

Conclusions

Remote sensing and GIS techniques applied to the Gebeit Al Maadin area, NE Su-dan, successfully delineated hydrothermal alteration zones using a range of digital image processing methods. These results hold significant implications for gold exploration in the region.

Landsat 8 OLI data, with spatial resolutions of 30 m (multispectral) and 15 m (panchromatic), and broad spectral coverage across the VNIR-SWIR regions, proved suitable for regional-scale mapping and preliminary mineral prospecting. However, it demonstrated limitations for more detailed mapping at medium or local scales. In contrast, ASTER data, which also provide 15 m and 30 m spatial resolutions, offer superior spectral resolution, particularly in the SWIR region. This enhanced spectral capability enables ASTER not only to delineate alteration zones but also to identify specific hydrothermal alteration minerals.

Alteration zones delineated using Landsat 8 OLI data appeared broader and more spatially dispersed than those derived from ASTER analysis. In

comparison, the narrower spectral bands of ASTER produced more precise results, allowing clearer discrimination of mineralogical variations. Consequently, alteration zones mapped using ASTER data were more accurate and more readily integrated into spatial analysis, making ASTER a more effective tool for mineral exploration.

References

- Abdelsalam MG, Robinson C, El-Baz F, Stern RJ. Applications of orbital imaging radar for geologic studies in arid regions: the Saharan testimony. Photogrammetric Engineering and Remote Sensing. 2000 Jun 1;66(6):717-26.
- Abdelsalam MG. Quantifying 3D post-accretionary tectonic strain in the Arabian–Nubian shield: superimposition of the Oko shear zone on the Nakasib suture, Red Sea Hills, Sudan. Journal of African Earth Sciences. 2010 Mar 1;56(4-5):167-78.
- Abrams M, Hook S, Ramachandran B. ASTER user handbook, version 2. Jet propulsion laboratory. 2002 Aug;4800:135.
- Abrams M. The Advanced Spaceborne Thermal Emission and Reflection Radiometer (ASTER): data products for the high spatial resolution imager on NASA's Terra platform. international Journal of Remote sensing. 2000 Jan 1;21(5):847-59.
- Alimohammadi M, Alirezaei S, Kontak DJ. Application of ASTER data for exploration of porphyry copper deposits: A case study of Daraloo–Sarmeshk area, southern part of the Kerman copper belt, Iran. Ore geology reviews. 2015 Oct 1;70:290-304.
- Almond DC, Ahmed F. Ductile shear zones in the northern Red Sea Hills, Sudan and their implication for crustal collision. Geological Journal. 1987 Dec;22(S2):175-84.
- Amer R, El Mezayen A, Hasanein M. ASTER spectral analysis for alteration minerals associated with gold mineralization. Ore Geology Reviews. 2016 Jun 1;75:239-51.
- Berger BR, Mars JL, Denning P, Phillips JD, Hammarstrom JM, Zientek ML, Dicken CL, Drew LJ, Seltmann R, Herrington RJ. Porphyry copper assessment of western Central Asia. US Geological Survey; 2014.
- Blondes MS, Gans KD, Thordsen JJ, Reidy ME, Thomas B, Engle MA, Kharaka YK, Rowan EL. US Geological Survey National produced waters geochemical database v2. 3 (PROVISIONAL). United States Geological Survey. 2016 Feb.
- Carrino TA, Crósta AP, Toledo CL, Silva AM, Silva JL. Geology and hydrothermal alteration of the Chapi Chiara prospect and nearby targets, southern Peru, using ASTER data and reflectance spectroscopy. Economic Geology. 2015 Jan 1;110(1):73-90.
- Cooley T, Anderson GP, Felde GW, Hoke ML, Ratkowski AJ, Chetwynd JH, Gardner JA, Adler-Golden SM, Matthew MW, Berk A, Bernstein LS. FLAASH, a MODTRAN4-based atmospheric correction algorithm, its application and validation. InIEEE international geoscience and remote sensing symposium 2002 Jun 24 (Vol. 3, pp. 1414-1418). IEEE.
- Crosta AP, De Souza Filho CR, Azevedo F, Brodie C. Targeting key alteration minerals in epithermal deposits in Patagonia, Argentina, using ASTER imagery and principal component analysis. International journal of Remote sensing. 2003 Jan 1;24(21):4233-40.
- 48 Crosta AP. Enhancement of Landsat Thematic Mapper imagery for residual soil mapping in SW Minas Gerais State Brazil, a prospecting case history in greenstone

- belt terrain. InProceedings of the 7[<] th> ERIM Thematic Conference on Remote
 Sensing for Exploration Geology, 1989 1989.
 - Crósta, A.P.; Moore, J. Enhancement of Landsat Thematic Mapper Imagery for Residual Soil Mapping in Sw Minas Gerais State, Brazil- a Prospecting Case History in Greenstone Belt Terrain. In Proceedings of the Seventh Thematic Conference on Remote Sensing for Exploration Geology: Methods, Integration, Solutions, Calgary, AB, Canada, 2–6 October 1989.
 - Debba P, Van Ruitenbeek FJ, Van Der Meer FD, Carranza EJ, Stein A. Optimal field sampling for targeting minerals using hyperspectral data. Remote Sensing of Environment. 2005 Dec 15;99(4):373-86.
 - El Khidir, S.O. and Babikir, I.A., 2013. Digital image processing and geospatial analysis of landsat 7 ETM+ for mineral exploration, Abidiya area, North Sudan. International journal of geomatics and geosciences, 3(3), pp.645-658.
 - EL Khidir, S.O.H., 2006. Remote sensing and GIS applications in geological mapping, prospecting for mineral deposits and Groundwater-Berber sheet area, northern Sudan (Doctoral dissertation, Al Neelain University).
 - Fitches WR, Graham RH, Hussein IM, Ries AC, Shackleton RM, Price RC. The late Proterozoic ophiolite of Sol Hamed, NE Sudan. Precambrian Research. 1983 Mar 1;19(4):385-411.
 - Fraser SJ, Green AA. A software defoliant for geological analysis of band ratios. International Journal of Remote Sensing. 1987 Mar 1;8(3):525-32.
 - Gupta RP. Remote sensing geology. Springer; 2017 Nov 24.

- Hunt GR, Ashley RP. Spectra of altered rocks in the visible and near infrared. Economic Geology. 1979 Nov 1;74(7):1613-29.
- Hunt GR. Near-infrared (1.3-2.4 mu m) spectra of alteration minerals; potential for use in remote sensing. Geophysics. 1979 Dec 1;44(12):1974-86.
- Johnson PR, Andresen A, Collins AS, Fowler AR, Fritz H, Ghebreab W, Kusky T, Stern RJ. Late Cryogenian–Ediacaran history of the Arabian–Nubian Shield: a review of depositional, plutonic, structural, and tectonic events in the closing stages of the northern East African Orogen. Journal of African Earth Sciences. 2011 Oct 1;61(3):167-232.
- Johnson PR, Kattan FH, Al-Saleh AM. Neoproterozoic ophiolites in the Arabian Shield: Field relations and structure. Developments in Precambrian Geology. 2004 Jan 1;13:129-62.
- Klemenic PM, Poole S. The geology and geochemistry of Upper Proterozoic granitoids from the Red Sea Hills, Sudan. Journal of the Geological Society. 1988 Jul:145(4):635-43.
- Kröner A, Greiling R, Reischmann T, Hussein IM, Stern RJ, Dürr S, Krüger J, Zimmer M. Pan-African crustal evolution in the Nubian segment of northeast Africa. Proterozic Lithospheric Evolution. 1987 Jan 1;17:235-57.
- Kruse FA, Lefkoff AB, Boardman JW, Heidebrecht KB, Shapiro AT, Barloon PJ, Goetz AF. The spectral image processing system (SIPS)—interactive visualization and analysis of imaging spectrometer data. Remote sensing of environment. 1993 May 1;44(2-3):145-63.
- Lillesand T, Kiefer RW, Chipman J. Remote sensing and image interpretation. John
 Wiley & Sons; 2015 Feb 18.
- 47 Lillesand T, Kiefer RW, Chipman J. Remote sensing and image interpretation. John
 48 Wiley & Sons; 2015 Feb 18.
- Loughlin WP. Principal component analysis for alteration mapping. Photogrammetric Engineering and Remote Sensing. 1991 Sep;57(9):1163-9.

- Mars JC, Rowan LC. Regional mapping of phyllic-and argillic-altered rocks in the Zagros magmatic arc, Iran, using Advanced Spaceborne Thermal Emission and Reflection Radiometer (ASTER) data and logical operator algorithms. Geosphere. 2006 May 1;2(3):161-86.
- Mwaniki MW, Möller MS, Schellmann G. A comparison of Landsat 8 (OLI) and Landsat 7 (ETM+) in mapping geology and visualising lineaments: A case study of central region Kenya. The International Archives of the Photogrammetry, Remote Sensing and Spatial Information Sciences. 2015 Apr 30;40:897-903.

- Ninomiya Y. A stabilized vegetation index and several mineralogic indices defined for ASTER VNIR and SWIR data. InIGARSS 2003. 2003 IEEE International Geoscience and Remote Sensing Symposium. Proceedings (IEEE Cat. No. 03CH37477) 2003 Jul 21 (Vol. 3, pp. 1552-1554). IEEE.
- Pour AB, Hashim M, Hong JK, Park Y. Lithological and alteration mineral mapping in poorly exposed lithologies using Landsat-8 and ASTER satellite data: Northeastern Graham Land, Antarctic Peninsula. Ore Geology Reviews. 2019 May 1;108:112-33.
- Pour AB, Hashim M, Park Y, Hong JK. Mapping alteration mineral zones and lithological units in Antarctic regions using spectral bands of ASTER remote sensing data. Geocarto International. 2018 Dec 2;33(12):1281-306.
- Pour AB, Hashim M. Identifying areas of high economic-potential copper mineralization using ASTER data in the Urumieh–Dokhtar Volcanic Belt, Iran. Advances in Space Research. 2012 Feb 15;49(4):753-69.
- Pour AB, Hashim M. The application of ASTER remote sensing data to porphyry copper and epithermal gold deposits. Ore geology reviews. 2012 Feb 1;44:1-9.
- Rajendran S, Nasir S, Kusky TM, Ghulam A, Gabr S, El-Ghali MA. Detection of hydrothermal mineralized zones associated with listwaenites in Central Oman using ASTER data. Ore geology reviews. 2013 Sep 1;53:470-88.
- Richards JA, Richards JA. Remote sensing digital image analysis. Berlin/Heidelberg, Germany: springer; 2022 Jan 6.
- Rowan LC, Hook SJ, Abrams MJ, Mars JC. Mapping hydrothermally altered rocks at Cuprite, Nevada, using the Advanced Spaceborne Thermal Emission and Reflection Radiometer (ASTER), a new satellite-imaging system. Economic Geology. 2003 Aug 1;98(5):1019-27.
- Rowan LC, Mars JC. Lithologic mapping in the Mountain Pass, California area using advanced spaceborne thermal emission and reflection radiometer (ASTER) data. Remote sensing of Environment. 2003 Mar 1;84(3):350-66.
 - Roy DP, Wulder MA, Loveland TR, Woodcock CE, Allen RG, Anderson MC, Helder D, Irons JR, Johnson DM, Kennedy R, Scambos TA. Landsat-8: Science and product vision for terrestrial global change research. Remote sensing of Environment. 2014 Apr 5;145:154-72.
- Sabins FF. Remote sensing for mineral exploration. Ore geology reviews. 1999 Sep 1;14(3-4):157-83.
- 43 Sabins Jr and Lulla, K., 1987. Remote sensing: principles and interpretation.
- Safari M, Maghsoudi A, Pour AB. Application of Landsat-8 and ASTER satellite remote sensing data for porphyry copper exploration: a case study from Shahr-e-Babak, Kerman, south of Iran. Geocarto international. 2018 Nov 2;33(11):1186-201.
- Seedorff, E., Dilles, J.H., Proffett, J.M., Einaudi, M.T., Zurcher, L., Stavast, W.J.,
 Johnson, D.A. and Barton, M.D., 2005. Porphyry deposits: Characteristics and
 origin of hypogene features.

- Shnain SK, Najm MN, Taher NA, Abdalrazzaq AS, Rashit B, Lishchyna V.
 Classification of Landsat 8 Images Using Convolutional Neural Network Based on Minimum Noise Fraction Transform. In2024 35th Conference of Open Innovations Association (FRUCT) 2024 Apr 24 (pp. 692-698). IEEE.
 Spatz DM, Wilson RT, Pierce FW, Bolm JG. Remote sensing characteristics of
 - Spatz DM, Wilson RT, Pierce FW, Bolm JG. Remote sensing characteristics of porphyry copper systems, western America Cordillera. Arizona geological society digest. 1995;20:94-108.
 - Stern RJ. Arc assembly and continental collision in the Neoproterozoic African Orogen: implications for the consolidation of Gondwanaland. Annual Review Of Earth And Planetary Sciences, Volume 22, pp. 319-351.. 1994;22:319-51.
 - Stern RJ. Crustal evolution in the East African Orogen: a neodymium isotopic perspective. Journal of African Earth Sciences. 2002 Apr 1;34(3-4):109-17.
 - Testa FJ, Villanueva C, Cooke DR, Zhang L. Lithological and hydrothermal alteration mapping of epithermal, porphyry and tourmaline breccia districts in the Argentine Andes using ASTER imagery. Remote Sensing. 2018 Jan 30;10(2):203.
 - Vail JR. Alkaline ring complexes in Sudan. Journal of African Earth Sciences (1983). 1985 Jan 1;3(1-2):51-9.
 - Van der Meer FD, Van der Werff HM, Van Ruitenbeek FJ, Hecker CA, Bakker WH, Noomen MF, Van Der Meijde M, Carranza EJ, De Smeth JB, Woldai T. Multi-and hyperspectral geologic remote sensing: A review. International journal of applied Earth observation and geoinformation. 2012 Feb 1;14(1):112-28.
 - Wulder MA, White JC, Goward SN, Masek JG, Irons JR, Herold M, Cohen WB, Loveland TR, Woodcock CE. Landsat continuity: Issues and opportunities for land cover monitoring. Remote Sensing of Environment. 2008 Mar 18;112(3):955-69.
 - Yamaguchi Y, Fujisada H, Kahle AB, Tsu H, Kato M, Watanabe H, Sato I, Kudoh M. ASTER instrument performance, operation status, and application to Earth sciences. InIGARSS 2001. Scanning the Present and Resolving the Future. Proceedings. IEEE 2001 International Geoscience and Remote Sensing Symposium (Cat. No. 01CH37217) 2001 Jul 9 (Vol. 3, pp. 1215-1216). IEEE.
 - Yamaguchi Y, Fujisada H, Kudoh M, Kawakami T, Tsu H, Kahle AB, Pniel M. ASTER instrument characterization and operation scenario. Advances in Space Research. 1999 Jan 1;23(8):1415-24.
 - Zeinelabdein KE, Albiely A. Ratio image processing techniques: a prospecting tool for mineral deposits, Red Sea Hills, NE Sudan. Int Arch Photogramm Remote Sens Spat Inf Sci. 2008;37:1295-8.
 - Zhang X, Pazner M, Duke N. Lithologic and mineral information extraction for gold exploration using ASTER data in the south Chocolate Mountains (California). ISPRS Journal of Photogrammetry and Remote Sensing. 2007 Sep 1;62(4):271-82.

Abbreviations

Abbreviations used in this paper include:

OLI Operational Land Imager
ASTER Advanced Spaceborne Thermal Emission and Reflection Radiometer

ANS Arabian Nubian Shield VNIR Visible / Near Infrared SWIR Shortwave Infrared TIR Thermal Infrared

TIRS Thermal Infrared Sensor

2025-6936-AJS - 4 NOV 2025

USGS United State Geological Survey Universal Transverse Mercator UTM

WGS World Geodetic System

Environment for Visualizing Images **ENVI**

Fast Line of sight Atmospheric Analysis of Spectral Hypercube **FLAASH**

MNF Minimum Noise Fraction

FOPCS Feature Oriented Principal Component Selection

PCA Principal Component Analysis

Digital Number DN Regions Of Interest ROI False Color Composite **FCC**

NNE North Northeast SSW South Southwest Spectral Angle Mapper SAM